

Quantitative phase imaging and complex field reconstruction by pupil modulation differential phase contrast

HANGWEN LU,* JAEBUM CHUNG, XIAOZE OU, AND CHANGHUEI YANG

Department of Electrical Engineering, California Institute of Technology, Pasadena, CA 91125, USA

*hllu@caltech.edu

Abstract: Differential phase contrast (DPC) is a non-interferometric quantitative phase imaging method achieved by using an asymmetric imaging procedure. We report a pupil modulation differential phase contrast (PMDPC) imaging method by filtering a sample's Fourier domain with half-circle pupils. A phase gradient image is captured with each half-circle pupil, and a quantitative high resolution phase image is obtained after a deconvolution process with a minimum of two phase gradient images. Here, we introduce PMDPC quantitative phase image reconstruction algorithm and realize it experimentally in a 4f system with an SLM placed at the pupil plane. In our current experimental setup with the numerical aperture of 0.36, we obtain a quantitative phase image with a resolution of 1.73 μm after computationally removing system aberrations and refocusing. We also extend the depth of field digitally by 20 times to $\pm 50\mu\text{m}$ with a resolution of 1.76 μm .

© 2016 Optical Society of America

OCIS codes: (100.5070) Phase retrieval; (170.0180) Microscopy; (110.3010) Image reconstruction techniques.

References and links

1. F. Zernike, "Phase contrast, a new method for the microscopic observation of transparent objects," *Physica* **9**, 686–698 (1942).
2. G. Nomarski, "Differential microinterferometer with polarized waves," *J. Phys. Radium* **16**(9), 9S–11S (1955).
3. D. Gabor, "A new microscopic principle," *Nature* **161**(4098), 777–778 (1948).
4. C. M. Vest, *Holographic Interferometry* (John Wiley and Sons, Inc., 1979).
5. I. Yamaguchi and T. Zhang, "Phase-shifting digital holography," *Opt. Lett.* **22**, 1268–1270 (1997).
6. R. Collier, *Optical holography* (Elsevier, 2013).
7. J. W. Goodman, *Introduction to Fourier optics* (Roberts and Company Publishers, 2005).
8. J. R. Fienup, "Phase retrieval algorithms: a comparison," *Appl. Opt.* **21** (15), 2758–2769 (1982).
9. G. Zheng, R. Horstmeyer, and C. Yang, "Wide-field, high-resolution Fourier ptychographic microscopy," *Nature photonics* **7**(9), 739–745 (2013).
10. X. Ou, R. Horstmeyer, C. Yang, and G. Zheng, "Quantitative phase imaging via Fourier ptychographic microscopy," *Opt. Lett.* **38**(22), 4845–4848 (2013).
11. L. Tian and L. Waller, "3d intensity and phase imaging from light field measurements in an led array microscope," *Optica* **2**, 104–111 (2015).
12. X. Ou, R. Horstmeyer, G. Zheng, and C. Yang, "High numerical aperture Fourier ptychography: principle, implementation and characterization," *Opt. Express* **23**(3), 3472–3491 (2015).
13. J. Chung, H. Lu, X. Ou, H. Zhou, and C. Yang, "Wide-field Fourier ptychographic microscopy using laser illumination source," <http://arxiv.org/abs/1602.02901>.
14. R. Horstmeyer, X. Ou, J. Chung, G. Zheng, and C. Yang, "Overlapped Fourier coding for optical aberration removal," *Opt. Express* **22**(20), 24062–24080 (2014).
15. S. Dong, R. Horstmeyer, R. Shiradkar, K. Guo, X. Ou, Z. Bian, H. Xin, and G. Zheng, "Aperture-scanning Fourier ptychography for 3D refocusing and super-resolution macroscopic imaging," *Opt. Express* **22**(11), 13586–13599 (2014).
16. X. Ou, J. Chung, R. Horstmeyer, and C. Yang, "Aperture scanning Fourier ptychographic microscopy," *Biomed. Opt. Express* **7**(8), 3140–3150 (2016).
17. N. Streibl, "Phase imaging by the transport equation of intensity," *Opt. Commun.* **49**(1), 6–10 (1984).
18. A. N. T. O. N. Barty, K. A. Nugent, D. Paganin, and A. Roberts, "Quantitative optical phase microscopy," *Opt. Lett.* **23**(11), 817–819 (1998).
19. C. J. R. Sheppard, "Defocused transfer function for a partially coherent microscope and application to phase retrieval," *J. Opt. Soc. Am. A* **21**, 828–831 (2004).
20. Z. Jingshan, R. A. Claus, J. Dauwels, L. Tian, and L. Waller, "Transport of intensity phase imaging by intensity spectrum fitting of exponentially spaced defocus planes," *Opt. Express* **22**(9), 10661–10674 (2014).

21. S. Bernet, A. Jesacher, S. Furhapter, C. Maurer, and M. Ritsch-Marte, "Quantitative imaging of complex samples by spiral phase contrast microscopy," *Opt. Express* **14**(9), 3792–3805 (2006).
22. D. K. Hamilton, and C. J. Sheppard, "Differential phase contrast in scanning optical microscopy," *Journal of microscopy* **133**(1), 27–39 (1984).
23. J. Mertz, A. Gasecka, A. Daradich, I. Davison, and D. Coté, "Phase-gradient contrast in thick tissue with a scanning microscope," *Biomed. Opt. Express* **5**, 407–416 (2014).
24. B. Kachar, "Asymmetric illumination contrast: a method of image formation for video light microscopy," *Science* **227**, 766–768 (1985).
25. S. B. Mehta, and C. J. Sheppard, "Quantitative phase-gradient imaging at high resolution with asymmetric illumination-based differential phase contrast," *Opt. Lett.* **34**(13), 1924–1926 (2009).
26. L. Tian, and L. Waller, "Quantitative differential phase contrast imaging in an LED array microscope," *Opt. Express* **23**(9), 11394–11403 (2015).
27. D. Lee, S. Ryu, U. Kim, D. Jung, and C. Joo, "Color-coded LED microscopy for multi-contrast and quantitative phase-gradient imaging," *Biomed. Opt. Express* **6**(12), 4912–4922 (2015).
28. L. Tian, J. Wang, and L. Waller, "3D differential phase-contrast microscopy with computational illumination using an LED array," *Opt. Lett.* **39**(5), 1326–1329 (2014).
29. S. Lowenthal, and Y. Belvaux, "Observation of phase objects by optically processed Hilbert transform," *Appl. Phys. Lett.* **11**(2), 49–51 (1967).
30. R. Hoffman and L. Gross, "Modulation Contrast Microscope," *Appl. Opt.* **14**, 1169–1176 (1975).
31. I. Iglesias, "Pyramid phase microscopy," *Opt. Lett.* **36**, 3636–3638 (2011).
32. Ashwin. B. Parthasarathy, K. K. Chu, T. N. Ford, and J. Mertz, "Quantitative phase imaging using a partitioned detection aperture," *Opt. Lett.* **37** (19), 4062–4064 (2012).
33. R. Barankov and J. Mertz, "Single-exposure surface profilometry using partitioned aperture wavefront imaging," *Opt. Lett.* **38**, 3961–3964 (2013).
34. I. Iglesias, and F. Vargas-Martin, "Quantitative phase microscopy of transparent samples using a liquid crystal display," *J. Biomed. Opt.* **18**(2), 026015–026015 (2013).
35. R. Barankov, J. C. Baritoux, and J. Mertz, "High-resolution 3D phase imaging using a partitioned detection aperture: a wave-optic analysis," *J. Opt. Soc. Am. A* **32**(11), 2123–2135 (2015).
36. R. A. Claus, P. P. Naulleau, A. R. Neureuther, and L. Waller, "Quantitative phase retrieval with arbitrary pupil and illumination," *Opt. Express* **23**, 26672–26682 (2015).
37. M. Bertero, and P. Boccacc, *Introduction to Inverse Problems in Imaging* (CRC, 1998).
38. S. Kubota and J. W. Goodman, "Very efficient speckle contrast reduction realized by moving diffuser device," *Appl. Opt.* **49**(23), 4385–4391 (2010).
39. R. Horstmeyer, R. Heintzmann, G. Popescu, L. Waller, and C. Yang, "Standardizing the resolution claims for coherent microscopy," *Nature Photonics* **10**(2), 68–71 (2016).
40. G. Zheng, X. Ou, R. Horstmeyer, and C. Yang, "Characterization of spatially varying aberrations for wide field-of-view microscopy," *Opt. Express* **21**, 15131–15143 (2013).
41. B. Bhaduri, K. Tangella, and G. Popescu, "Fourier phase microscopy with white light," *Biomed. Opt. Express* **4**(8), 1434–1441 (2013).
42. Z. Wang, L. Millet, M. Mir, H. Ding, S. Unarunotai, J. Rogers, M. U. Gillette, and G. Popescu, "Spatial light interference microscopy (SLIM)," *Opt. Express* **19**, 1016–1026 (2011).
43. G. Popescu, T. Ikeda, R. R. Dasari, and M. S. Feld, "Diffraction phase microscopy for quantifying cell structure and dynamics," *Opt. Lett.* **31**, 775–777 (2006).

1. Introduction

While traditional microscopy only captures the intensity, an object's phase information is highly desired in many situations. For example, most biological tissues are transparent and rich structural information is contained in phase. To obtain the samples' phase, many techniques have been developed. Widely used phase gradient methods such as Zernike phase contrast microscope [1] and Nomarski's differential interference contrast (DIC) [2] are able to get qualitative phase contrast images. However, in both techniques, phase and intensity information are mixed in the images and therefore the phase measurement is not quantitative. Holography [3–7] is another phase imaging method where the object's wavefront interferes with a reference beam and the phase information is obtained from the recorded interference pattern. However, holography suffers from coherent speckle noise and it requires a complicated optical system to generate the path-length matched reference beam. Phase information can also be retrieved by using computational algorithms [8]. For example, Fourier ptychographic microscopy (FPM) takes a series of images captured under different illumination angles [9–13] or different overlapped

apertures [14–16] to iteratively recover a sample's phase and amplitude; transport of intensity phase imaging [17–20] uses images captured at different defocused planes to solve the transport of intensity equation (TIE) and retrieve phase. The large number of measurements needed is a disadvantage of these methods. Spiral phase contrast microscopy [21] is another effective quantitative phase imaging method that uses a spiral phase plate for modulation in the Fourier plane. Unlike FPM, it requires only three images at different plate orientations. However, limited spatial coherence negatively influences the absolute phase value accuracy.

Besides the methods mentioned above, differential phase contrast (DPC) is another effective way to get quantitative phase images. In comparison to the majority of the other methods, DPC is experimentally simple to implement. In DPC, spatially asymmetrical imaging methods are applied to generate a phase gradient image [22–26, 28], and a sample's quantitative phase information can also be reconstructed by deconvolving the phase gradient images with the phase transfer function [22, 25, 26, 28]. In previous studies, DPC images are achieved in different approaches. D. K. Hamilton et. al first demonstrated DPC in scanning optical microscopy by splitting the detector's area into two halves and detecting the phase gradient by intensity integral difference between the two half sections [22]. Scanning-free asymmetrical illumination DPC (AIDPC) techniques were later demonstrated. Ref. [25] blocks half of the illumination plane for each captured image. Ref. [26] use a programmable LED matrix to generate the phase gradient images. High resolution, speckle-free, quantitative phase images were reconstructed computationally with deconvolution algorithm. Using colored LEDs, dark field, bright field and DPC phase images can also be captured in one shot [27]. However, these methods still have limitations. They only work well for thin samples since oblique illumination components will result in different lateral shifts for different z-planes in thick samples and 2D Fourier shift relation is no longer valid. Although 3D DPC method to overcome this limitation is demonstrated by Lei Tian et. al [28], this approach requires images to be taken separately for each single LED and results in worse reconstructed resolution with increasing defocusing distance.

Besides asymmetric illumination, asymmetric Fourier plane modulation can also generate phase contrast images of a sample. A very simple way is Foucault method which uses a knife to block half of the Fourier plane to view the phase gradient. Lowenthal et al. imaged aberrated wavefront and heated air phase changes with a Hilbert filter on the Fourier plane [29]. Hoffman et al. reported modulation contrast microscope which can generate a qualitative phase gradient image with Fourier plane modulation [30]. In this technique, partially coherent light from a slit illuminates the sample and modulated on the Fourier plane. The sample's phase gradient perpendicular to the slit is reflected on the image intensity. However, this is not quantitative phase interpretation and attenuation caused by scattering and absorption is mixed up with phase information. Further improvements on the modulation contrast microscopy were reported later. Pyramid phase microscopy (PPM) [31] applies a pyramid to split the Fourier plane into four subsections, forming four phase gradient images on the detector. Assisted with a calibration of a known sample, phase gradients along two perpendicular directions are reconstructed and quantitative phase can be further obtained. The pyramid can also be replaced with quatrefoil lens [32, 33] or a liquid crystal display (LCD) [34], named partitioned detection aperture (PDA). In all of the above methods with asymmetric Fourier plane modulation, the illumination numerical aperture (NA_i) determines the detectable dynamic range of phase gradient and is preferable when NA_i is equal to $NA/2$. Only smooth phase gradients can be correctly recorded, and phase gradient beyond the dynamic range suffers from saturation problem. These phase gradient imaging methods are also partially coherent methods. Although the modified algorithm for out-of-focus samples based on PDA system is introduced in [35], the depth of field can not be extended with full resolution due to partial coherence limitation.

Addressing the above limitations, we develop a pupil modulation differential phase contrast (PMDPC) imaging method. We use a spatial light modulator (SLM) to modulate a 4f imaging

system's pupil plane. However, instead of detecting the phase gradient as done in other phase modulation methods [30–34], we generate the phase transfer function to reconstruct the phase directly, similar to [25,26,36]. Unlike aforementioned partially coherent phase imaging methods [24–28,30–36], we use spatially coherent illumination to obtain a quantitative phase image and demonstrate that we can dramatically extend the depth of field of our system computationally. The sample is not restricted to be smoothly varying and quantitative phase can be reconstructed without calibration.

In PMDPC, a phase gradient image forms at the image plane when half of the pupil plane is blocked by the SLM. Using two such phase gradient images captured separately by applying complementary half-circle pupils with the SLM, we can construct a DPC image that carries the sample's phase information. With DPC images, a quantitative phase image of the sample can be reconstructed with a deconvolution procedure. Further, we are able to combine this quantitative phase with the sample's intensity image to obtain the complete field of the sample which then allows us to post-process the image. We report experimentally that aberrations arising from the optical elements in the system can be corrected by deconvolving the reconstructed image with a pre-calibrated pupil function. We can also digitally extend the depth of field using angular spectrum propagation algorithm [7]. With our current PMDPC imaging setup with the numerical aperture (NA) of 0.36, a quantitative phase image with a resolution of $1.73\mu\text{m}$ is obtained. The depth of field for a $20\times$ objective is increased digitally by 20 times as well.

In section 2, we describe the basic principles of PMDPC with simulation results. PMDPC's requirement of the weak object approximation and formation of a full complex field of a sample are also included in this section. We present the experimental setup in section 3. We show the experiment results in section 4, including quantitative phase imaging results of microbeads, resolution measurement with a Siemens star target, depth of field improvement and a biological imaging example of a frog blood sample. At the end of this section, we also compare the reconstructed image qualities given different numbers of input images and compare the result with FPM. Finally, we discuss the advantages and disadvantages of PMDPC compared other techniques and mention potential improvements in section 5.

2. Basic principles

2.1. Weak object transfer function

Consider the following 4f imaging system shown in Fig. 1(a). A complex sample [Fig. 1(b)] is placed at the front focal plane of lens l_1 . The sample is illuminated by a collimated coherent light. The light field reaching the back focal plane of l_1 would map out the Fourier spectrum of the sample. An SLM placed at this Fourier plane modulates the sample's Fourier spectrum with half-circle pupil patterns [Fig. 1(c)]. This modulated Fourier spectrum is inverse-Fourier transformed by l_2 to form a phase gradient image [Fig. 1(d)] on a CCD camera placed at the back focal plane of l_2 .

To simplify our analysis, we set the magnification ratio as 1 : 1 by assuming l_1 and l_2 to have the same focal length. The mathematical relations are as follows: the object field $o(x, y)$ is Fourier transformed by l_1 to become its Fourier spectrum $O(u, v)$. $O(u, v)$ is then modulated by a coherent pupil function $P(u, v)$, resulting in the complex distribution $O(u, v)P(u, v)$ at the pupil plane. $O(u, v)P(u, v)$ is inverse-Fourier transformed by l_2 to form a phase gradient image $I(x, y)$ which is captured by the camera:

$$I(x, y) = \left| \mathcal{F}^{-1} \{ \mathcal{F} \{ o(x, y) \} P(u, v) \} \right|^2. \quad (1)$$

The Fourier transform of $I(x, y)$ is equal to the autocorrelation of $O(u, v)P(u, v)$:

$$\tilde{I}(u, v) = [O(u, v)P(u, v)] * [O^*(-u, -v)P^*(-u, -v)] \quad (2)$$

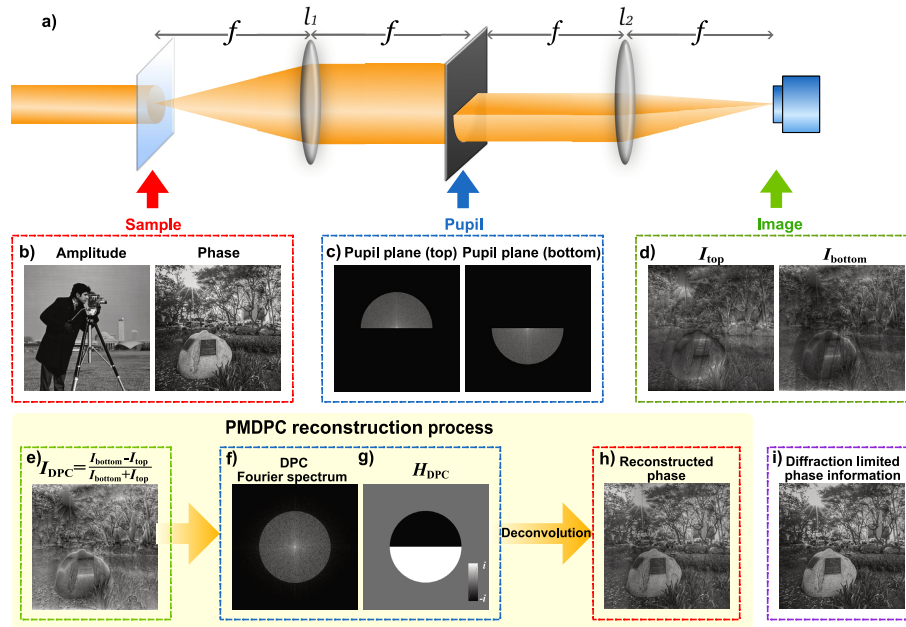


Fig. 1. Principle of PMDPC algorithm. (a) A 4f optical system setup with an adjustable pupil. A simulated complex sample (b) is placed at the front focal plane of L_1 and modulated at pupil plane by half-circle pupil functions (c), forming phase gradient images on camera (d). In PMDPC reconstruction process, I_{DPC} (e) is constructed by phase gradient images. The Fourier spectrum of I_{DPC} (f) is deconvolved with DPC transfer function (g). Reconstructed phase (h) is obtained after deconvolution process following Eq. (10). The PMDPC reconstructed phase is comparable with diffraction limited phase information of the sample (i).

$$\tilde{I}(u, v) = \iint O(u - \xi, v - \eta) O^*(-\xi, -\eta) P(u - \xi, v - \eta) P^*(-\xi, -\eta) d\xi d\eta. \quad (3)$$

Like other phase retrieval algorithms [22, 25–28, 36], we use the weak object assumption here. In other words, we approximate the complex object as $o(x, y) = e^{-\alpha(x, y) + i\phi(x, y)} \approx 1 - \alpha(x, y) + i\phi(x, y)$, where α is the absorption coefficient and ϕ is the phase induced by the sample. In Fourier domain, it becomes $O(u, v) \approx \delta(u, v) - A(u, v) + i\Phi(u, v)$. In the expansion of $O(u - \xi, v - \eta) O^*(-\xi, -\eta)$ in Eq. (3), the cross-terms can be assumed to be negligible according to the weak object assumption. Finally, we can separate the phase and amplitude components, and rewrite Eq. (3) as:

$$\tilde{I}(u, v) = P(0)P^*(0)\delta(u, v) + H_{amp}A(u, v) + H_{ph}\Phi(u, v), \quad (4)$$

where $A(u, v)$ and $\Phi(u, v)$ are the Fourier spectrum of $\alpha(x, y)$ and $\phi(x, y)$, respectively. And H_{amp} and H_{ph} are the amplitude and phase transfer functions defined as:

$$H_{amp} = -[P(u, v)P^*(0) + P(0)P^*(-u, -v)], \quad (5)$$

$$H_{ph} = i[P(u, v)P^*(0) - P(0)P^*(-u, -v)]. \quad (6)$$

2.2. DPC image formation and reconstruction

DPC reconstruction process is shown in Figs. 1(e)–1(h): DPC image I_{DPC} is constructed using phase gradient images I_1 and I_2 that are captured with a pair of complimentary half-circle pupils P_1 and P_2 :

$$I_{DPC} = \frac{I_1 - I_2}{I_1 + I_2}. \quad (7)$$

Since the pupil functions satisfy $P_1(u, v) = P_2(-u, -v)$, the amplitude transfer functions $H_{1,amp}$ and $H_{2,amp}$ cancel each other while the phase transfer functions are doubled, rendering the following relation in the Fourier domain:

$$\tilde{I}_{DPC}(u, v) = H_{DPC}(u, v)\Phi(u, v), \quad (8)$$

\tilde{I}_{DPC} is the Fourier transform of I_{DPC} and

$$H_{DPC}(u, v) = \frac{H_{1,ph}(u, v) - H_{2,ph}(u, v)}{2P(0)P^*(0)}. \quad (9)$$

For a weak object, the absorption can be assumed to be negligible compared to the zero frequency component, and is omitted in the denominator [26]. \tilde{I}_{DPC} can be obtained from captured images, and H_{DPC} is determined by the pupil functions. Therefore, the sample's phase distribution can be reconstructed by a direct deconvolution process according to the following equation [26, 27, 37]:

$$\phi_r(u, v) = \mathcal{F}^{-1} \left\{ \frac{\sum_j H_{j,DPC}^*(u, v) \tilde{I}_{j,DPC}(u, v)}{\sum_j |H_{j,DPC}|^2 + \epsilon} \right\}, \quad (10)$$

where ϵ is an infinitesimal number added for regularization ($\epsilon = 10^{-6}$ is applied in both experiment and simulation). The summation in Eq. (10) takes into account multiple pairs of pupil functions in the reconstruction process.

It has been previously shown that multi-axis illumination pairs are necessary in AIDPC algorithm since a large portion of the Fourier spectrum information near the asymmetric axis in DPC transfer function is missing [26]. This missing information results in large reconstruction errors in corresponding spatial frequencies (for example, if only top and bottom illuminations are applied, reconstruction errors take the form of vertically distributed strips). However, we show that this multi-axis requirement is not necessary in PMDPC. As shown in Fig. 1(g), PMDPC transfer function covers the whole non-zero frequency region within NA with the same transmission magnitude. The only missing region is the zero frequency center which only affects the offset value of the reconstructed phase image. The zero-frequency component is always transmitted without attenuation in both half-circle pupils. Appendix A discusses in detail about this center frequency treatment. Experimental misalignment and numerical errors may result in inaccuracy along asymmetric axis. Therefore having more pupil pairs improves phase reconstruction accuracy by averaging the reconstruction results to decrease numerical error. However, one pair of asymmetric pupils is sufficient in most cases for a quantitative phase image using PMDPC. In the following experiments, we still apply 2-axis pupil modulation unless otherwise stated. At the end of section 4, the reconstructed phase images of 1-axis versus 2-axis pupil modulation are shown and reconstruction errors are calculated compared against FPM reconstructed phase images.

2.3. Weak object requirement

As mentioned above, PMDPC algorithm uses the weak object assumption $o(x, y) = e^{-\alpha(x, y) + i\phi(x, y)} \approx 1 - \alpha(x, y) + i\phi(x, y)$. Samples with large phase differences will cause

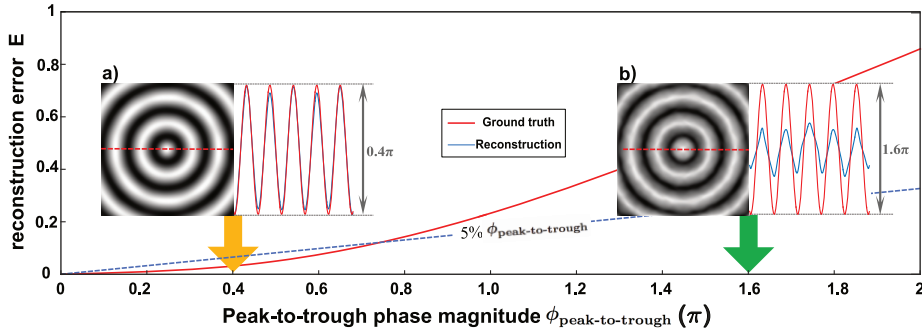


Fig. 2. Red solid line plots the relationship between the reconstruction error, E and the peak-to-trough phase magnitude of the sample, $\phi_{peak-to-trough}$. Blue dashed line indicates where $E/\phi_{peak-to-trough}$ equals to 5%. When $\phi_{peak-to-trough} \leq 0.74\pi$, $E/\phi_{peak-to-trough}$ is below 5%. Inserted figures (a) and (b) show the PMDPC reconstructed phase images when $\phi_{peak-to-trough}$ equals to 0.4π and 1.6π , respectively. The ground truth and reconstructed phase profile along the red dashed line are also plotted in both cases on the right side.

residue errors due to this approximation. It is reasonable to expect that when the phase difference becomes larger than a certain value, the reconstruction result may no longer be quantitative. To explore this limit, we simulate a concentric sinusoidal phase object with different peak-to-trough phase magnitudes, and then apply PMDPC reconstruction algorithm. Here, eight pairs of pupils are applied to minimize numerical errors. Reconstructing error E is calculated as the standard deviation from true value expressed as [14]:

$$E = \frac{1}{N} \sqrt{\sum_{x,y} |\phi - \phi_r + \alpha|^2} \quad (11)$$

where ϕ is the ground truth phase. In simulation, we take ϕ as NA-limited phase information, and in experimental results, it stands for FPM phase reconstruction. ϕ_r is the reconstructed phase image, and N is the number of pixels in the image. Since the offset value of phase can be arbitrary and will strongly affect the calculated E , a parameter, α is applied to compensate for the offset difference and is defined as $\alpha = \frac{1}{N} \sum_{x,y} (\phi_r - \phi)$.

Reconstruction error E of different $\phi_{peak-to-trough}$ values is shown in Fig. 2 with red solid line. At the same time, we show in blue dashed line where E equals to 5% of $\phi_{peak-to-trough}$. When the peak-to-trough phase magnitude $\phi_{peak-to-trough}$ is smaller than 0.74π , the reconstruction error E is below 5%. For $\phi_{peak-to-trough} \geq 0.74\pi$, E increases more and more rapidly and the reconstruction is no longer quantitatively accurate. However, we notice in Fig. 2 that even when the weak object assumption is invalid, we are still able to obtain qualitative phase images with the PMDPC algorithm.

2.4. Forming a complex object field with the reconstructed phase and measured intensity

After having reconstructed the quantitative phase information of a weakly scattering sample, synthesizing the sample's full complex field is readily possible with the addition of its intensity measurement. When an image of the sample is captured with a fully opened pupil in the 4f system of Fig. 1, it contains the amplitude information, $|o(x, y)|$, of the sample in its intensity measurement, $I(x, y)$, such that

$$I(x, y) = |o(x, y)|^2. \quad (12)$$

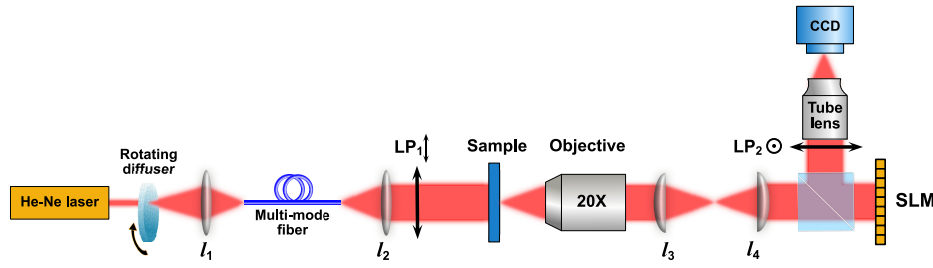


Fig. 3. PMDPC Experimental setup. Light from a He-Ne laser passes through a rotating diffuser and l_1 , coupled into a multimode fiber. l_2 collimates the beam coming out of the fiber which then incidents the sample. Light from the sample is collected by the objective (Olympus $20\times 0.4\text{NA}$, $f = 9\text{mm}$). The objective's focal plane is relayed by lenses l_3 and l_4 to the surface SLM (liquid crystal on silicon display, model: Holoeye LC-R 1080, refresh rate: 60Hz). The modulated light passes through the tube lens (Thorlabs ITL200, $f = 200\text{mm}$) to form a phase gradient image on the CCD. LP_1 and LP_2 are polarizers with perpendicular polarization directions to achieve the SLM's amplitude modulation.

With this information, the sample's full complex field, $o(x,y)$ can be reconstructed because it is simply a multiplication of the sample's amplitude and phase information:

$$o(x, y) = |o(x, y)|e^{i\phi(x,y)} = \sqrt{I(x, y)} e^{i\phi(x,y)}. \quad (13)$$

In our experiments, we measure our sample's intensity after the PMDPC measurements to reconstruct the sample's complex field and perform post-processing to computationally correct for aberrations and refocus to different z-planes.

3. Experimental setup

The experimental realization of PMDPC system is shown in Fig. 3. Light from a He-Ne laser source passes through a rotating diffuser and couples into a multimode fiber in order to suppress coherent speckle noise [16, 38]. The light from the multimode fiber is collimated and incidents normally on the sample. The randomized light from the multimode fiber can be considered as spatially coherent since NA_i is sufficiently small (Appendix B). The sample's optical field is collected by an objective (Olympus $20\times 0.4\text{NA}$, $f = 9\text{mm}$). A reflective SLM is placed at the pupil plane, which is also the back focal plane of the objective. Since the focal plane of the objective lies inside of the objective, a 4f relay system consisting of lens l_3 and l_4 are applied to image the pupil plane onto the SLM's surface. Pupil modulation is achieved by the SLM (LCOS display Model: Holoeye LC-R 1080, refreshing rate: 60Hz), whose fast axis is oriented 45 degrees from the two perpendicularly oriented polarizers LP_1 and LP_2 . The SLM generates phase shift between its two axes for the modulated pixels, thus rotating light polarization by 90 degrees. The modulated components of the SLM reflected light is selected with LP_2 . Finally, a tube lens (Thorlabs ITL200, $f = 200\text{mm}$) focuses the modulated light onto a CCD camera (Allied Vision: Prosilica GX6600, $5.5\mu\text{m}$ pixel size, 4Hz frame rate) and phase gradient images are captured to be used for our reconstruction algorithm.

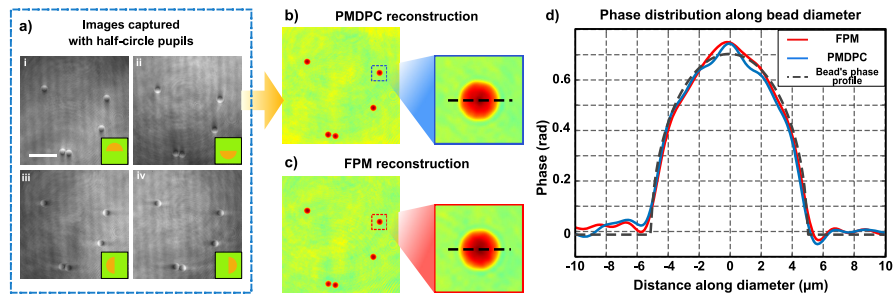


Fig. 4. PMDPC phase reconstruction result of $10\mu\text{m}$ microbeads. (a) shows vertical and horizontal phase gradient image pairs and corresponding pupil functions. (b) and (c) are PMDPC and FPM reconstructed phase images and right side of them are zoom-in images of the boxed square. (d) plot the phase distribution along the black dashed line across the bead diameter of both reconstructed results and microbead sample's estimated phase profile. (scale bar: $50\mu\text{m}$)

4. Experimental results

4.1. Quantitative phase imaging with microbeads

A quantitative phase images of a $10\mu\text{m}$ polystyrene microbead sample is imaged to show PMDPC's quantitative phase reconstruction capability. $10\mu\text{m}$ microbeads are immersed in oil ($n = 1.580$) at room temperature. Eight pairs of phase gradient images are captured to minimize numerical error and misalignment. Figure 4(a) shows vertical and horizontal image pairs and corresponding pupil functions. Reconstructed phase images of PMDPC are shown in Fig. 4(b). Phase reconstruction of the same region is conducted with FPM [14–16] for comparison as well, shown in Fig. 4(c). We compare PMDPC reconstructed phase with FPM retrieved phase information and plot the phase distribution along one of the beads' diameter in Fig. 4(d). We also plot the estimated ideal phase profile of a microbead from the reconstruction result. Our measurements indicate that the refractive index of microbead is 1.587, which is consistent with the refractive index of polystyrene.

4.2. Spatial resolution measurement with Siemens star phase target

PMDPC imaging results of phase Siemens star target is shown in Fig. 5. The Siemens star resolution phase target, recommended by [39] is fabricated on a gold-coated glass. Using focused ion beam (FIB), the Siemens star pattern is first etched onto the gold surface and then a $50\mu\text{m}$ by $50\mu\text{m}$ area encompassing the whole pattern is further etched with the same exposure time until the glass substrate is exposed within the entire area.

As introduced in section 2.4, we capture four phase gradient images [Fig. 5(a)] and another full-aperture intensity image [Fig. 5(c-ii)] in experiment. Quantitative phase [Fig. 5(c-i)] is reconstructed following PMDPC reconstruction process illustrated in Figs. 1(e)–1(h). The reconstructed phase, after combined with captured intensity, forms the complex optical field distribution of the sample being imaged.

Up to now, the resolution of reconstructed phase is blurred by defocusing and other system aberrations [Fig. 5(c)]. However, the fact that we have computed the complex field distribution implies that we can computationally post-process the images to remove the aberrations. We characterized the aberration using the method described in [40]. Multiple manually defocused images of $1\mu\text{m}$ micro-bead are captured, and the optimization algorithm is applied to determine the correct values of different Zernike modes. Figure 5(e) shows the phase image after decon-

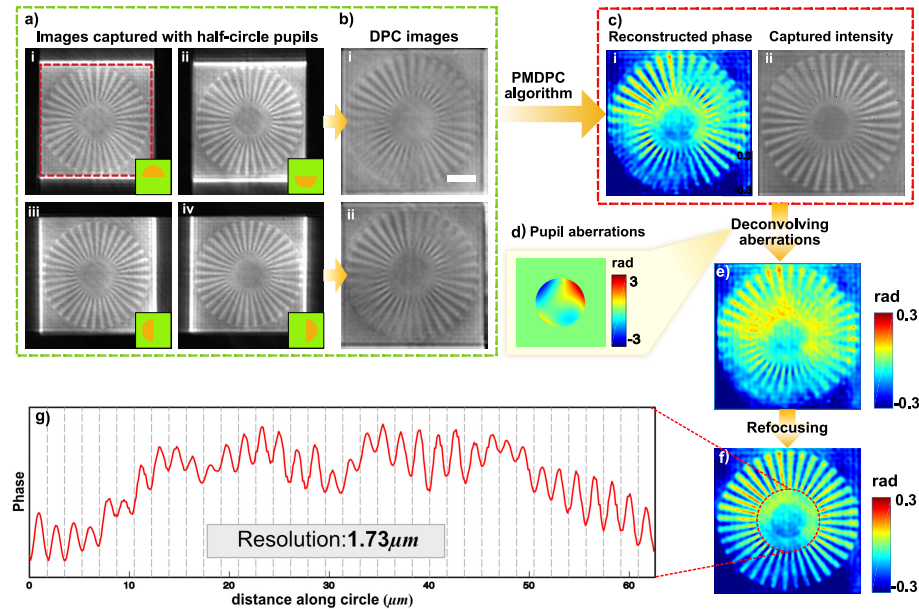


Fig. 5. Siemens star phase target resolution calibration process. (a) shows captured phase gradient images and corresponding pupil functions. DPC images (b) of each pupil pair are constructed following equation 7. (c) shows PMDPC reconstructed phase (i) and captured intensity (ii). (e) shows the phase image after deconvolution with calibrated pupil aberrations mapped in (d). (f) is the phase image after refocusing to the sample plane. (g) plots the phase distribution along the dashed circle in (f). (scale bar: $10\mu\text{m}$)

volving the reconstructed optical field with the characterized aberration function [Fig. 5(d)]. Finally, we apply angular spectrum propagation method to digitally propagate the images into focus. Figure 5(f) shows an aberration-corrected in-focus phase image. Figure 5(g) plots the phase distribution along the red dashed circle in Fig. 5(f), indicating a periodic phase resolution of $1.73\mu\text{m}$, which matches with the theoretical resolution

$$\frac{\lambda}{NA} = \frac{633\text{nm}}{0.36} = 1.75\mu\text{m}. \quad (14)$$

With the object's complex field, we are also able to computationally adjust the focus to different z -planes, thereby digitally extending the depth of field of the system. To demonstrate this, we take the same Siemens star target and manually defocus it in z -direction to $\pm 50\mu\text{m}$ and $\pm 100\mu\text{m}$. We can observe in Fig. 6(a) that captured defocused images are completely blurred at these planes. PMDPC reconstructed optical field distribution at the defocus distance of $-48\mu\text{m}$ is shown in Fig. 6(b) as an example. The complex field distribution at the image plane is a diffraction pattern generated by the Siemens star pattern and also the square edge. After aberration correction and refocusing process described in Fig. 5, sharply focused phase images are formed. Figures 6(c)–6(f) show the refocused images and resolution measurements for each defocus distance. When the sample is defocused by $-48\mu\text{m}$ and $+47\mu\text{m}$, the periodic resolution of refocused phase images reaches $1.76\mu\text{m}$, which closely matches the theoretical resolution. And when the sample is defocused to $-96\mu\text{m}$ and $+96\mu\text{m}$, the refocused image's resolution drops to $1.84\mu\text{m}$ and $2.22\mu\text{m}$, respectively.

The standard depth of field of $20\times$ microscope objective is $5.6\mu\text{m}$ defined by $\lambda/NA^2 + e/(M \cdot NA)$, where e is the camera's pixel size and M is the system's magnification factor. In compari-

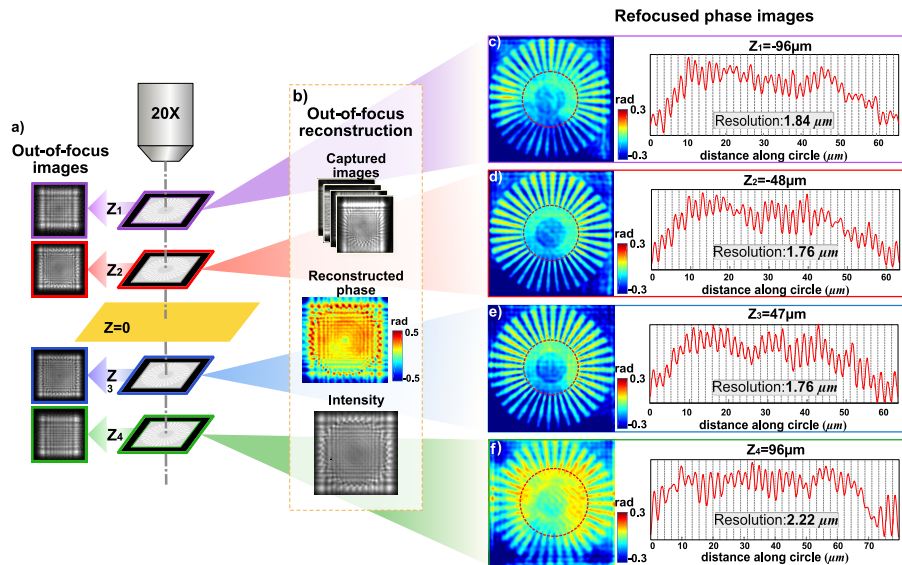


Fig. 6. Depth of field extension demonstration. Intensity images captured under 20 \times , 0.4NA objective when Siemens star phase target is defocused to different z planes are shown in (a) correspondingly. (b) shows the sample reconstruction results when $z = -48\mu\text{m}$, where resolution is greatly blurred due to defocusing. (c)–(f) are the phase images after digitally propagating back to the sample plane. Phase distributions along the dashed red circles are plotted on the right side of each image separately.

son, our method increases the depth of field digitally by more than 20 times.

It was pointed out in previous work that AIDPC only applies for thin samples on the focal plane. However, PMDPC is able to reconstruct phase of thick samples and defocused samples with consistent resolution. The difference is explained as follows: AIDPC reconstruction algorithm [25, 26] is based on partially coherent illumination, which relies on the 2D Fourier spectrum shifting property under oblique illuminations. This mathematical relation only applies for the sample information on the system's focal plane. Defocused information suffers from problems such as image lateral shift and broadened point spread function, and therefore cannot be correctly reconstructed. Efforts were made in previous AIDPC to reconstruct 3D phase images [28], where images are captured by turning on each single LED in the illumination matrix and then laterally shifted accordingly during reconstruction process. However, this modified method has some problems. First, it requires images to be captured for each single LED, which implies longer acquisition time. Second, it only achieves $6\mu\text{m}$ resolution under 20 \times objective when the sample is defocused to $50\mu\text{m}$ because of broadened PSF at defocused planes. In comparison, PMDPC uses a collimated beam to illuminate the sample. Therefore, the relation of 2D Fourier shifting for different illumination angles is no longer required, and the resolution degradation and lateral shifting are non-issues for the PMDPC method.

4.3. Imaging biological samples

We also tested the performance of PMDPC in biological samples. Figure 7 shows the image of a frog blood cell sample. Reconstructed phase and intensity are shown in Figs. 7(a) and 7(b) following the same procedures as above. Under red light illumination, the cells are almost transparent, and only nuclei are clearly seen in the intensity image, while the phase image can

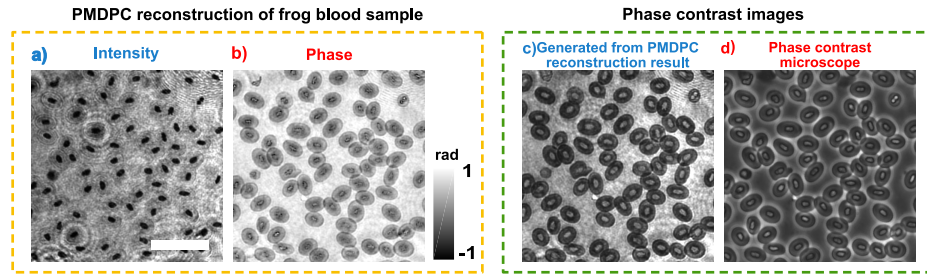


Fig. 7. PMDPC image of frog blood sample. (a) and (b) are reconstructed intensity and phase distributions obtained following the procedure in Fig. 5. Phase contrast image (c) is generated with the reconstructed field. The same area of the sample is also imaged under a conventional phase contrast microscope for comparison, shown in (d). (scale bar: $50\mu m$)

better resolve the shape of blood cells and the fine structures around nuclei. We can also generate a phase contrast image by shifting the central spatial frequency of the reconstructed field by to obtain the result shown in Fig. 7(c). At the same time, we capture an image of the same region under a phase contrast microscope, shown in Fig. 7(d). We observe that the phase contrast image generated from PMDPC reconstruction does not suffer from halo and shade-off effects that exist in conventional phase contrast microscopy. Meanwhile, PMDPC image has higher background noise since it is a coherent optical system. We notice that the peak-to-trough phase magnitude of the frog blood cell sample is slightly beyond the quantitative reconstruction region determined in section 2.3. This result shows that PMDPC is still a reasonable qualitative phase imaging technique even when weak object assumption is not accurate in some cases.

4.4. Required number of measurements versus image quality

Based on analysis in section 2.2, we stated that PMDPC can still reconstruct good phase image with only one pair of asymmetric pupils. To illustrate this, we reconstruct the phase images of Siemens phase star target, frog blood cells sample and microbeads sample using one pair of phase gradient images and two pairs separately, shown in the first two rows in Fig. 8(a). Reconstruction difference are shown in last row of Fig. 8(a). Comparing the images in both cases, there is no significant missing-frequency artifact when using one pair of phase gradient images for reconstruction. The reconstruction difference can be attributed to experimental misalignment, numerical artifacts, and other imperfections. We also compare the microbead sample reconstructed phase images with FPM reconstructed phase, and calculate the reconstruction error E in Fig. 8(b). In both cases, reconstruction errors are less than 10% of original $\phi_{peak-to-trough}$. Reconstruction with 2 pairs of images is slightly more accurate than with 1 pair. The reconstruction error with 8 pairs is 0.0389 for the reconstructed phase image shown in Fig. 4(b). We expect that more image pairs help improve algorithm robustness and suppress noise. In situations where less images and faster capturing process are needed, only two phase gradient images and one intensity image is sufficient for complex field reconstruction and refocusing process as demonstrated in this paper.

5. Discussion

We have introduced PMDPC, a phase imaging method via asymmetric pupil modulation. Quantitative high resolution phase images can be reconstructed with a minimum of one pair of phase gradient images captured with complimentary half-circle pupils. After simple post-process procedures of aberration deconvolution and refocusing, we achieve phase imaging with resolution

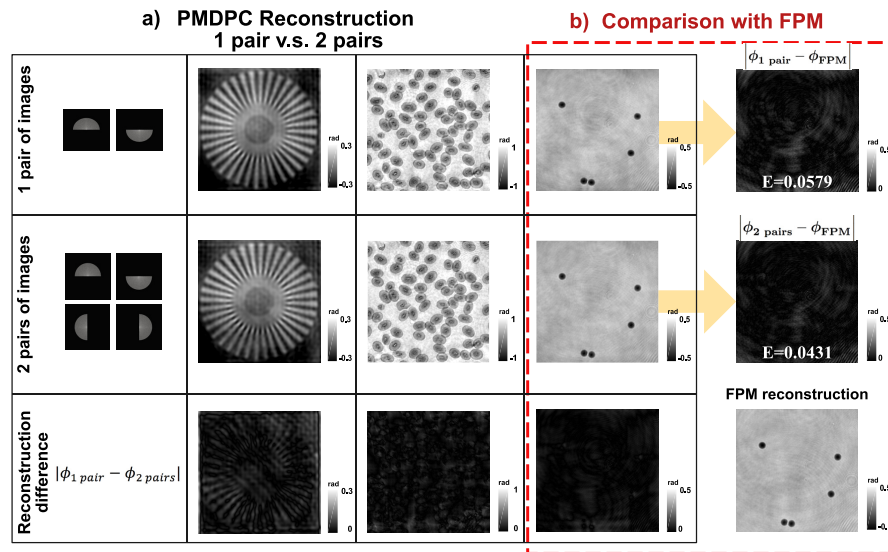


Fig. 8. Phase imaging with different numbers of measurements. The first two rows in (a) show PMDPC reconstruction results using one pair and two pairs of phase gradient image measurements, respectively. The difference between the reconstruction results are shown in the third row. Comparison with FPM reconstruction is shown in (b) with microbead sample. Reconstruction error, E is shown for both 1-pair and 2-pairs reconstruction results.

of $1.73\mu\text{m}$ given the system NA of 0.36. By digitally propagating the reconstructed field, we can also extend the depth of field of a $20\times$, 0.4NA objective to $\pm 50\mu\text{m}$ with almost no resolution deterioration, which is more than a 20-fold improvement compared to a conventional microscope.

Unlike other phase gradient imaging methods [30–34], PMDPC doesn't suffer from phase gradient saturation problem. Therefore, it is also suitable for non-smooth samples. Compared with AIDPC described in [25, 26], PMDPC has larger depth of field and requires less captured images. We also expect that PMDPC is more robust against Gaussian noise because it has uniform magnitude of phase transfer function across the entire aperture whereas the weak magnitude of AIDPC's transfer function in high-frequency region results in poor signal-to-noise ratio (SNR). The drawback of PMDPC is that it has higher background noise. Although we are able to suppress speckle noise by using a rotating diffuser in our PMDPC system, the coherent illumination means that it is still more sensitive to dust or other imperfections in the optical path compared to partial coherent illumination where extended light sources are employed. The phase detection sensitivity of PMDPC is related with SNR and the sample's attenuation, which is analyzed in detail in Appendix C. In our experimental setup, the sensitivity is measured to be 0.034rad , corresponding to the optical length of $\lambda/200$.

PMDPC is achieved in a simple $4f$ system that can be incorporated into a conventional microscope with a setup similar to partitioned detection aperture [34] and Fourier Phase Microscope in [41]. The resolution of PMDPC is limited by the system NA and imaging speed is determined by the camera frame rate, SLM refreshing rate and light intensity. Currently, it takes us 32 seconds to capture an image. The slow frame rate is due to low irradiance on sample, at $1.5 \times 10^{-4}\text{W}/\text{m}^2$. This problem is caused by low illumination efficiency rather than PMDPC algorithm since zero frequency information is always totally transmitted. It can be solved by increasing light couple efficiency, using higher power output light source, and using a higher

NA collimation lens l_2 . In addition, the reflective SLM can be changed into transmissive SLM to avoid energy loss caused by beam splitter. In addition, this work is focused on the demonstration of PMDPC method and performance, and there is much room for optimization and improvement.

To decrease the cost and improve light efficiency and capturing speed, the SLM can be replaced with alternative modulation methods since only half-circles amplitude modulation is required. For example, we can place a rotating half-circle mask at the pupil plane to achieve the same modulation function as SLM, which can be much faster and cheaper. In summary, PMDPC can be a cost-effective, high-speed, and high-quality quantitative phase imaging technique that can find usage in various fields such as biology, etc..

Appendix A: Zero-frequency component treatment

The treatment of zero frequency is very important. Since we are using spatially coherent illumination, the zero frequency information is a very small spot in the Fourier domain. This spot should always be allowed to transmit without attenuation. This is because in the algorithm Eqs. (4)–(6), zero-frequency information, $P(0)$, is involved and is non-zero. Therefore, if the zero-frequency is blocked, the algorithm will fail. To keep zero-frequency information passing through the modulator, we always keep a small region at the center opened in the modulation pattern displayed on the SLM, and the size of the opening matches with the size of the zero frequency's extent in our system, as shown in the following Fig. 9(a). Since the light source (the end of multimode fiber) is imaged to Fourier plane, the zero frequency diameter can be calculated as:

$$d_{zero-frequency} = \frac{f_{obj}}{f_2} \times d_{fiber} = \frac{9mm}{45mm} \times 300\mu m = 60\mu m \quad (15)$$

where d_{fiber} is the fiber diameter, f_{obj} is the focal length of objective lens, and f_2 is the focal length of collimation lens l_2 in 3. With SLM pixel size of $8.1\mu m$, this zero-frequency size corresponds to 8 pixels in diameter and 4 pixels in radius. Therefore, the center pixels within radius of 4 are kept open on SLM [Fig. 9(b)]. The information on the center will be canceled finally when constructing. Therefore, it is best to choose the smallest center opening that contains the zero-frequency to minimize the loss of phase information.

Based on the above analysis, the alignment of SLM is very important. In the experiment, the center can be easily determined. We capture four images with top, bottom, left, and right half-circle patterns. If the center opening diameter is chosen as four pixels, only when the SLM's center overlaps with the zero-frequency center, the four images are balanced and all show up as bright field images. Otherwise, we can tune the center pixel position in MATLAB code until they are balanced.

Appendix B: Discussion on finite NA_i

We use a multimode fiber as the light source output and a rotating diffuser to generate random phases that change over time. Therefore, during the exposure time, the speckle patterns from different modes are averaged on the detector to provide a uniform background. A multimode fiber instead of a singlemode fiber is used because we need different propagating modes in the fiber to interfere at the image plane to provide multiple speckle patterns which can cancel each other during the exposure time. However, the multimode fiber has a relatively larger core diameter of $300\mu m$, and is not strictly spatial coherent as assumed in the algorithm. The following simulations will show the tolerance of NA_i to use our coherent imaging model during reconstruction. We generate a sample with $\phi_{peak-to-trough} = 0.6\pi$ [Fig. 10(a)]. Figure 10(b) shows the reconstruction result when the sample is illuminated with coherent plane wave ($NA_i = 0.001$, 1 pixel in Fourier domain). We also simulate a finite- NA_i illuminated sample and

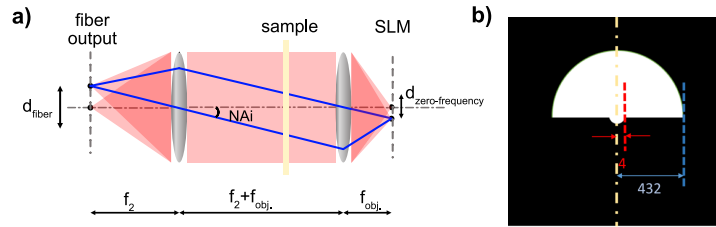


Fig. 9. Illumination NA analysis. (a) shows the relation of NA_i with Fourier plane. The fiber end is imaged to SLM plane with a magnification ratio of f_{obji}/f_2 . (b) shows the SLM display pattern considering the finite NA_i in experiment (not scaled to real size, only for demonstration to show the center clearly, unit: pixel).

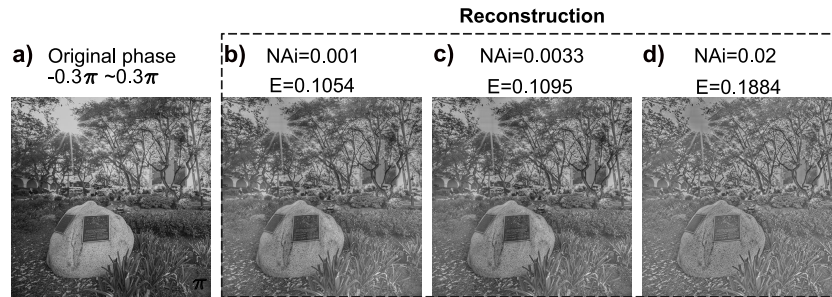


Fig. 10. Finite NA_i simulation. (a) is sample's original phase, (b)–(d) are reconstruction results with different illumination NA. Reconstruction errors, E are calculated with Eq. (11).

carry out the reconstruction algorithm. The simulation follows our experimental setup, where $NA_i = d_{\text{fiber}}/f_2 = 0.0033$. Simulated FoV is $384\mu\text{m} \times 384\mu\text{m}$, and the center opening in Fourier modulator is chosen to match NA_i . The reconstruction result is shown in Fig. 10(c). As can be seen, there is no significant difference observed in the reconstruction between $NA_i = 0.0033$ and $NA_i = 0.001$. Reconstruction errors E are also calculated, shown in Fig. 10. Therefore, we are able to assume this finite- NA_i in our experiment as a coherent illumination.

However, when NA_i becomes much larger, we cannot consider it as coherent illumination anymore. For example, when $NA_i = 0.02$, the reconstruction of the same sample will deteriorate as shown in Fig. 10(d). In this case, an algorithm with partially coherent illumination imaging model is needed, which was described in [26, 36].

Appendix C: Discussion on phase sensitivity

A system's sensitivity defines the minimum detectable phase, which is closely related with noise level. For interferometric phase imaging methods, a stronger reference beam can improve SNR, while PMDPC is a non-interferometric phase imaging methods that relies on the captured SNR itself.

We first limit our discussion to transparent samples. With no noise and infinite bit depth,

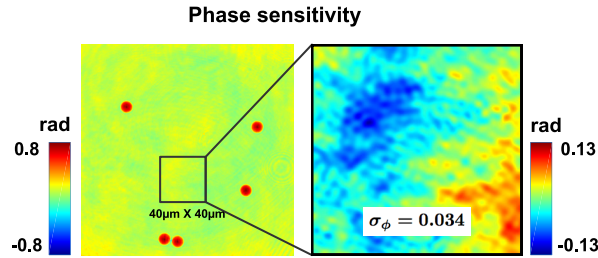


Fig. 11. PMDPC phase sensitivity. A 40×40 region is selected in the reconstructed phase image, where no features are present. The sensitivity is calculated as 0.034 rad.

ideally PMDPC is able to resolve infinitely small phase change. However, when noise exists, a real imaging sensor is considered, and the phase change is small, the contrast in the captured phase gradient images will be very low. When noise level is larger than signal contrast, the method cannot detect the phase change. When noise exists and the sample has no attenuation, Eq. (4) reduces to:

$$\tilde{I}(u, v) = |P(0)|^2 \delta(u, v) + H_{ph} \Phi(u, v) + \tilde{n}(u, v). \quad (16)$$

In detection domain, it converts into

$$I(x, y) = 1 + \mathbf{H}\{\phi\}(x, y) + n(x, y), \quad (17)$$

where \mathbf{H} denoting Hilbert transform because the phase transfer function is actually a Hilbert modulator. $\tilde{n}(u, v)$ is the Fourier transform of noise, $n(x, y)$. Since any function can be decomposed into sine functions and for simplicity, we discuss on a 1-D sine function, with phase distribution $\phi(x) = \beta \sin(kx)$. Since Hilbert transform of $\sin(kx)$ is $\mathbf{H}\{\sin(kx)\} = -\cos(kx)$, detected signal on the image plane will be $I \approx 1 - \beta \cos(kx) + n(x)$. When the noise level $n(x)$ is comparable with β , the detected signal fluctuation will be obscured by the noise. When $\beta > n$, phase signal can be detected.

For example, when $P_{signal}/P_{noise} = 1/n = 100$, (SNR = 20dB), detectable phase signal variation β should be larger than $0.01 \approx 0.003\pi$, corresponding to $1nm$ optical length for wavelength of $632.8nm$. Therefore, the DPC method is still very sensitive to the phase changes.

For samples with attenuation, the phase sensitivity also depends on the attenuation. When phase changes are very small, while attenuation is much larger than phase changes, the cross-term in expression of O^*O cannot be neglected. In this case, reconstructed phase will be mixed with sample's attenuation information. Approximately, when the phase difference is above 1/10 of the attenuation factor, this artifact is almost non-noticeable.

For our setup, we measure phase sensitivity by selecting a region of $40 \times 40 \mu m^2$ (167×167 sensor pixels) where no features are present and calculating the standard deviation of the reconstructed phase over this region. The same method is used in [42, 43]. The reconstructed phase fluctuation in this region is shown in Fig. 11. The experimental sensitivity of PMDPC is 0.034 rad, corresponding to the optical length of $\lambda/200$, which is comparable to other coherent phase imaging methods such as diffraction phase microscopy (DPM) [43].

Funding

NIH (grant no. R01 AI096226); CII 2015 (grant no. 32070065).

Acknowledgments

The authors would like to thank Daniel Martin for fabricating the Siemens star phase target, and thanks to Jinho Kim, Joshua Brake and Haowen Ruan for discussions and help with experiments.